Journal of Materials Chemistry A

ROYAL SOCIETY OF CHEMISTRY

PAPER

View Article Online
View Journal | View Issue

Cite this: J. Mater. Chem. A, 2025, 13, 29610

A polysulfide/ferricyanide redox flow battery with extended cycling†

Mahla Sarfaraz Khabbaz,[a] Anupma Thakur,[b] Dipak Maity,[c] Sepideh Biabanialitappeh,[a] Bhargava Mortha,[a] Joshua P. McKay,[a] Gerardo Parada,[a] Mangilal Agarwal,[c] Honghu Zhang,[d] Xin Zhang,[e] J. David Bazak[e] and Xiaoliang Wei *[ab]

The inexpensive sulfur raw material is promising to enable cost-effective redox flow batteries for long duration energy storage. But the catastrophic through-membrane crossover of polysulfides remains a severe challenge resulting in irreversible performance degradation and short cycle life. In this work, we demonstrate that use of a permselective cation exchange membrane yields a two orders of magnitude enhancement in polysulfide retention compared to the benchmark Nafion membrane. Combined physico-chemical, spectroscopic, and microscopic analyses suggest more disordered sidechain structures, which lead to the more hydrophobic nature and smaller hydrophilic domains in the membrane. The microstructural features contribute to the effective mitigation of polysulfide crossover. As a result, the cycle life of polysulfide/ferricyanide flow cells is boosted over a substantially extended test time. This finding sheds light on the fundamental membrane factors that cause polysulfide permeation and can provide feasible directions in the development of permselective membranes for polysulfide flow batteries.

Received 3rd July 2025
Accepted 20th July 2025

DOI: 10.1039/d5ta05404d

rsc.li/materials-a

1. Introduction

The key challenges for grid resilience include integration of fluctuating energy sources, management of more dynamic loadings, and establishment of power supply security, all requiring robust long-duration energy storage.[1] Moreover, the wide adoption of emerging high-profile artificial intelligence (AI) technologies strictly requires non-interrupted operation of large-scale data centers to maintain data security.[2] As one of the most recognized solutions, redox flow batteries (RFBs) are particularly attractive for stationary energy storage at scale to address these challenges.[3,4] RFBs' major advantages of superior scalability and flexibility originate from the spatial separation of energy and power in their unique cell architecture. The energy-bearing redox materials are dissolved in liquid electrolytes and energy conversion reactions occur only when the electrolytes are circulated through porous electrodes. The cost and durability of redox materials mostly dictate the market potential of an RFB system.[5] All-vanadium RFBs are the state-of-the-art system, but the high vanadium cost is a prohibitive factor against scaled commercialization.[6] Organic redox materials are being extensively investigated for both aqueous and nonaqueous RFBs,[7–9] but meanwhile face critical challenges of long-term chemical instability, common need of an inert atmosphere, and/or debatable cost estimation. These drawbacks have largely hampered the practical uptake of these RFB systems.

Elemental sulfur is an inexpensive material sourced mainly from petroleum refining and natural gas processing. Sulfides including monosulfide and short-chain polysulfides (S_x^{2-}, x = 1–4) are among the classical inorganic anolyte redox materials used in aqueous RFBs.[10–12] These sulfides generally have high solubilities (>2 M) with two transferred electrons and are highly promising for achieving high energy density in their RFBs. However, sulfide-based RFBs have limited success in commercialization. As the only example with commercial-scale (12 MW/120 MWh) installations, Innogy's polysulfide/bromine flow battery (PSB) projects were all terminated before commissioning.[13] One of the near-fatal drawbacks is the irreversible crossover of sulfide species. Even the benchmark cation exchange membranes (CEMs) such as Nafion have failed to prevent sulfide crossover to the catholyte side, resulting in sulfide loss from the anolyte, solid sulfur precipitation at the

[a]School of Mechanical Engineering, Purdue University, 723 West Michigan Street, Indianapolis, IN, 46202, USA. E-mail: wei304@purdue.edu
[b]School of Materials Engineering, Purdue University, 701 West Stadium Avenue, West Lafayette, IN, 47907, USA
[c]Integrated Nanosystems Development Institute, Indiana University Indianapolis, 625 West Michigan Street, Indianapolis, IN, 46202, USA
[d]National Synchrotron Light Source-II, Brookhaven National Laboratory, Upton, New York 11973, USA
[e]Physical and Computational Sciences Directorate, Pacific Northwest National Laboratory, 3340 Stevens Drive, Richland, WA 99354, USA

† Electronic supplementary information (ESI) available. See DOI: https://doi.org/10.1039/d5ta05404d

catholyte, and eventually performance failure. With single or directly stacked Nafion membranes, stable capacity could be achieved for short cycling only and long-duration operation was often unsuccessful.[14–18] To address this issue, advanced membrane approaches have been investigated to increase permselectivity against sulfides. Lu *et al.* developed a charge-reinforced ion-selective (CRIS) membrane formed with porous carbon coatings on a Nafion membrane.[19] This CRIS membrane took advantage of the strong sulfide adsorption to form an electro-repulsive permeation barrier to retain sulfides, which enabled a KI/K_2S_2 flow cell to demonstrate stable cycling for ~3 months. Chen *et al.* adopted a similar strategy using an electrocatalyst embedded membrane electrode assembly (MEA) to achieve extended stable cycling for a Na_2S_2/$Na_4Fe(CN)_6$ flow cell.[20,21] A dual membrane configuration with parallel aligned CEM and AEM was used in an alkaline polysulfide-air flow cell, but seriously fluctuating efficiency and an increased cell overpotential were observed.[22] Chiang *et al.* employed a Li^+-exclusive superionic conducting (LiSICON) ceramic membrane in an air-breathing polysulfide RFB system,[23] but the membrane suffers from a critical drawback of limited scalability because of low conductivity, poor mechanical strength, and high cost. Considering these drawbacks, the development of advanced sulfide-blocking membranes is an urgently needed area for enabling long cycling polysulfide-based RFBs.

In this work, we report extended stable cycling for an aqueous near-neutral RFB system using a Na_2S_2 anolyte and $K_3Fe(CN)_6$ catholyte (denoted as S/Fe), enabled by a cost-effective Fumasep F1850 membrane with enhanced permselectivity over polysulfides. The ferro/ferricyanide redox couple is one of the most commonly used catholyte materials for aqueous RFBs with well-defined electrochemical properties.[24,25] Combined physico-chemical, spectroscopic, and microscopic characterizations of this membrane indicate higher hydrophobicity and smaller sizes of hydrophilic regions, potentially imparted by the greater extent of structural disorder in the sidearm compared to the benchmark Nafion. This microstructural feature contributes to the favored improvement in polysulfide retention by two orders of magnitude, better than that of Nafion. The S/Fe flow cells demonstrated near-constant capacity for as long as 300 cycles, which corresponds to 49 days, with the fade rate as low as 0.176% per day.

2. Experimental

2.1 Materials and methods

Sodium sulfide nonahydrate ($Na_2S{\cdot}9H_2O$, ≥98.0%), sulfur (S, purified by sublimation, ~100 mesh particle size), cobalt(II) nitrate hexahydrate ($Co(NO_3)_2{\cdot}6H_2O$, 99%), potassium chloride (KCl, ≥99.0%), sodium chloride (NaCl, ≥99.0%), and sodium hydroxide (NaOH, ≥98%) were purchased from Sigma-Aldrich. Potassium ferricyanide ($K_3Fe(CN)_6$, 99+%) and cobalt(II) chloride hexahydrate ($CoCl_2{\cdot}6H_2O$, 98%) were purchased from Fisher. The Fumasep F1850 membrane was purchased from the Fuel Cell Store (Bryan, TX). The Nafion 115 membrane (N115) was purchased from Ion Power (Tyrone, PA). SIGRACELL® graphite felts (GFD2.5, 2.5 millimeters thick) were purchased from SGL Carbon (Germany).

2.2 Crossover test

The through-membrane crossover rates of redox materials were measured using H-shaped permeation cells. The F1850 and N115 membranes were converted to K^+/Na^+ form by successively heating in 3 wt% H_2O_2 at 80 °C for 1 h, washing with deionized water, heating in 1 M H_2SO_4 at 80 °C for 1 h, washing with deionized water, soaking in 1 M KOH/NaOH at room temperature for 24 h, and washing with deionized water.

The setup consisted of a 0.5 M source solution (15 mL) on one side and inert permeate solution (15 mL) on the other side, sandwiching the tested membrane. For Na_2S_2, 1 M NaCl was used as the permeate solution to balance ionic strength and minimize osmotic pressure. For $K_3Fe(CN)_6$, 1.5 M KCl was used as the permeate. The effective area of the disk-shaped membrane was 0.78 cm^2. Both sides of the H cell were magnetically stirred. At specified time intervals, 3 mL samples were taken from both sides and the permeate side samples were subjected to ultraviolet-visible (UV-vis) measurements using a Thermo Scientific Evolution 600 spectrometer. Following Beer's law, their absorbance peak intensities were interpolated to the pre-determined intensity-concentration calibration plot to obtain the evolving crossover concentrations. The through-membrane permeability, P, was determined according to eqn (1) below:[19]

$$\mathrm{Ln}\left(1-\frac{C_t}{C_0}\right)=-\frac{AP}{TV}t \quad (1)$$

where t is the test time, C_t is the crossover concentration in the permeate at time t, C_0 is the initial concentration in the source (0.5 M), A is the effective area (0.78 cm^2), T is the membrane thickness, and V is the volume of the permeate (15 mL). P was obtained from the slope of the linear relationship of $-\mathrm{Ln}\left(1-\frac{C_t}{C_0}\right)$ with t.

2.3 Membrane characterization

2.3.1 Water uptake (WU) and swelling ratio (SR). The two K^+ form membranes were dried in a vacuum oven at 40 °C for 24 h and were immersed in deionized water for another 24 h. The WU was calculated using eqn (2):

$$\mathrm{WU}=\frac{m_{\mathrm{wet}}-m_{\mathrm{dry}}}{m_{\mathrm{dry}}}\times 100 \quad (2)$$

where m_{dry} and m_{wet} are the weights of the dry and wet membranes, respectively. Meanwhile, the SR was calculated using eqn (3):

$$\mathrm{SR}=\frac{A_{\mathrm{wet}}-A_{\mathrm{dry}}}{A_{\mathrm{dry}}}\times 100 \quad (3)$$

where A_{dry} and A_{wet} are the areas of the dry and wet membranes, respectively.

2.3.2 Ionic conductivity. A 6.6 cm^2 flow cell without including carbon electrodes was used to measure the ionic

conductivity of K^+ form membranes with 3 M KCl electrolyte circulated at both sides. Electrochemical impedance spectroscopy (EIS) was used to measure the ohmic resistances (*i.e.*, the high frequency intercept in the obtained Nyquist plot) with and without the presence of a membrane (N115 or F1850); the difference between them is the resistance (R) of the membrane. The conductivity (σ) of the membrane was calculated using eqn (4) below:

$$\sigma = \frac{T}{A \times R} \quad (4)$$

where T and A are the thickness and the effective area (*i.e.*, 6.6 cm^2), respectively, of the membrane.

2.3.3 Contact angle. The K^+ forms of N115 and F1850 membranes were dried in a vacuum oven at 40 °C for 24 h. Their contact angles were measured using a ramé-hart 200-F4 goniometer.

2.3.4 Atomic force microscopy (AFM). The surface morphology of these membranes was investigated using a Cypher VRS microscope (Asylum Research, CA) in tapping mode using a Fastscan B probe (Bruker, CA). N115 and F1850 were rinsed thoroughly with deionized water and dried in a vacuum oven at 40 °C for 24 h prior to imaging. Scans were conducted at ambient conditions over areas of 1 μm × 1 μm. The scanning rate was 2 Hz with a resolution of 256 points × 256 lines. The images were processed using Igor software to evaluate surface roughness and feature dimensions.

2.3.5 Field emission scanning electron microscopy (FE-SEM). The K^+ forms of N115 and F1850 were dried in a vacuum oven at 40 °C for 24 h. Gold coating was carried out using a Denton Desk V Sputter Coater. FE-SEM images and energy-dispersive X-ray (EDX) spectroscopy/mapping of gold-coated membranes and graphite felt electrodes were collected using a JEOL JSM-7800F microscope.

2.3.6 Magic angle spinning-nuclear magnetic resonance (MAS-NMR). ^{19}F MAS-NMR spectroscopy was conducted with a Bruker 2.5 mm HXY probe operating on a 600 MHz (14.7 T) Avance III HD spectrometer with temperature regulation at a software set-point of 298 K. The membrane samples were carefully sliced into ~2 mm × 2 mm segments using a doctor blade, and these were loaded into the MAS rotors such that the basal planes of the pieces would centrifuge against the rotor wall on spinning. Spectra were referenced to aqueous 0.1 M sodium trifluoroacetate at −75.4 ppm,[26] which was also used for ^{19}F pulse calibration and yielded a π/2 pulse of 3.4 μs.

MAS-NMR was primarily conducted at 30 kHz, with additional spinning rates of 15 kHz and 20 kHz used to confirm the isotropic peak assignments. ^{19}F spectra were acquired with a Hahn echo, with the net echo delay (194 μs) set to achieve a refocusing time of four rotational periods. Whole-echo acquisition was used with a brief dead time (6.5 μs) and the resulting free-induction decay was left-shifted to the refocusing point using ssNake v1.4 (which was also employed for peak deconvolution, including all spinning sidebands).[27] All echoes were recorded with 256 scans, a spectral width of 200 kHz, an acquisition time of 10.2 ms, and a recycle delay of 30 s. Pseudo-Voigt line shapes were used for all deconvolutions, with both isotropic shift and Lorentzian/Gaussian linewidth components for all peaks regressed against the experimental data. Signal fractions were based on addition of all associated spinning side bands to the corresponding isotropic peak areas. ^{19}F–^{13}C cross-polarization spectra were also acquired, with the Hartmann–Hahn match condition determined empirically using N115 and a contact time of 1.5 ms, utilizing rotor-synchronized π-pulse decoupling on the ^{19}F channel during the acquisition period.[28]

2.3.7 Attenuated total reflectance Fourier-transform infrared spectroscopy (ATR-FTIR). ATR-FTIR spectra of N115 and F1850 membranes were collected using a Thermo Scientific Nicolet iS5 spectrometer equipped with an iD7-ATR accessory with a diamond crystal. The membranes were cut into 5 mm × 5 mm samples and then directly placed on the ATR crystal plate.

2.4 Cyclic voltammetry (CV)

Using a CHI660D potentiostat (CH Instrument, Austin, TX), CV curves were measured in a three-electrode setup consisting of an Ag/AgCl (saturated KCl) reference electrode, GFD2.5 strip counter electrode, and glassy carbon working electrode. Electrolyte solutions of 50 mM redox materials in 1 M supporting NaCl or KCl were used. A potential sweeping rate of 5 mV s^{-1} was chosen for all CV scans. For the Na_2S_2 anolyte, Co catalyst particles were electro-deposited on the glassy carbon surface by maintaining the potential at −0.05 V below the reduction peak potential of Co^0/Co^{2+} redox for 20 seconds in a source solution of 50 mM $CoCl_2$ in 1 M NaCl.

Kinetic measurement of $K_3Fe(CN)_6$ was performed using its CV curves at different potential sweeping rates v ranging from 10 to 100 mV s^{-1}. The diffusion coefficient (D) was determined *via* the Randles–Sevcik equation (eqn (5)):[29]

$$i_p = 0.4463\ (nF)^{3/2} AC(vD/RT)^{1/2} \quad (5)$$

where i_p is the peak current, n is the number of transferred electrons, F is the Faraday constant (96 485 C mol^{-1}), A is the electrode area (0.071 cm^2), C is the $K_3Fe(CN)_6$ concentration, T is the temperature, and R is the gas constant (8.314 J K^{-1} mol^{-1}). D was obtained from the slope of the linear $i_p - v^{1/2}$ relationship. The electron transfer rate constant (k_0) was obtained *via* the Nicholson analysis (eqn (6) and (7)):

$$\Psi = (-0.6288 + 0.0021\Delta E_p)/(1 - 0.017\Delta E_p) \quad (6)$$

$$\Psi = k_0(\pi DnF/RT)^{-1/2} v^{-1/2} \quad (7)$$

where Ψ is the kinetic parameter and ΔE_p is the peak separation. The k_0 was calculated from the slope of the linear $\Psi - v^{-1/2}$ plot.

2.5 Flow cell test

The GFD2.5 electrode used in the $K_3Fe(CN)_6$ catholyte was thermally treated in an air atmosphere at 400 °C for 6 h to increase the wettability. Cobalt–decorated GFD2.5 (Co/GFD2.5) was used to catalyze the polysulfide redox, following prior efforts.[14,30,31] The Co/GFD2.5 was prepared *via* successive steps: boiling in 1 M NaOH for 1 h and washing with deionized water,

soaking in 1 M $Co(NO_3)_2$ solution for 24 h and drying in an oven at 80 °C, and finally calcining in a 4% H_2/argon atmosphere at 800 °C for 8 h with a ramp rate of 3.5 °C min^{-1} (Carbolite Gero furnace, 1700 °C model). The Co loading in the obtained Co/GFD2.5 was 11.6 mg cm^{-2}.

The bolted S/Fe flow cells consisted of graphite plate enclosures, thermally treated GFD2.5 at the catholyte, Co/GFD2.5 at the anolyte, and a membrane in between with an active area of 6.6 cm^2. The K^+ form membrane was soaked in deionized water for 24 h before cell assembly. The catholyte was 10 mL of 1 M $K_3Fe(CN)_6$ and the anolyte was 15 mL of 1 M Na_2S_2. Based on the loaded electrolytes, the polysulfide utilization was low corresponding to only 33% even at 100% state of charge (SOC) of the flow cells. The electrolytes were circulated at a flow rate of 20 mL min^{-1} using a Masterflex® L/S® peristaltic pump (Cole-Parmer, Vernon Hills, IL). Electrochemical impedance spectroscopy (EIS) was used to measure the Nyquist plots and derive the area specific resistance (ASR) of the flow cells with a Solartron SI 1287A electrochemical interface with an SI 1250E frequency response analyzer (Scribner Associates, Southern Pines, NC). A constant current mode with voltage control was used to cycle the flow cells at room temperature with a Neware CT-4008 battery tester (Belleville, IL).

3. Results and discussion

3.1 Crossover tests

Fumasep F1850 is a non-reinforced, 50-micron-thick CEM with a nominal equivalent weight (EW) of 1800 g mol^{-1}, which is manufactured from a perfluorosulfonic acid polymer resin with long side chains. In comparison, the benchmark baseline Nafion membranes have an EW of 1100 g mol^{-1} and a thickness of 127 microns. The F1850 membrane has demonstrated substantially decreased crossover of methanol and vanadium ions in direct methanol fuel cells and all-vanadium RFBs, respectively.[32–34] In addition, an attractive benefit of F1850 is its cost-effectiveness. F1850 has a potential to achieve membrane cost reduction by a factor of 4 compared to N115.[34] Considering the significant contribution of the membrane to the overall RFB stack cost,[35] F1850 holds good promise to decrease the capital expenditure for system installation on large scales.

To evaluate its effectiveness in improving the S/Fe RFB, the permeation rates of Na_2S_2 and $K_3Fe(CN)_6$ through this membrane were measured using H-type permeation cells (Fig. 1a). The evolving crossover concentrations in the permeate side were quantified by UV-vis spectroscopy. The UV-vis spectra as a function of concentration and the obtained peak intensity-concentration calibration curves for the two redox materials are shown in Fig. S1a, b, S2a and b in the ESI.† Fig. 1b and c show the measured UV-vis spectra of Na_2S_2 permeating through N115 and F1850 membranes, respectively. It is noted that there are two major absorbance peaks in the UV-vis spectra of dilute Na_2S_2 solutions. The dominant one at 300 nm belongs to S_2^{2-} and the minor one at 372 nm can be assigned to S_4^{2-}. This agrees well with the previous UV-vis reports on species speciation in polysulfide solutions.[16,19] The main reason for the coexistence of multiple polysulfide ions is their similar Gibbs free energies resulting in complicated chemical equilibria of mixed disproportionation/comproportionation reactions.[36,37] The electrolyte composition is concentration dependent and other polysulfide species such as S_3^{2-} were also detected using Raman spectroscopy in more concentrated polysulfide solutions.[20,21]

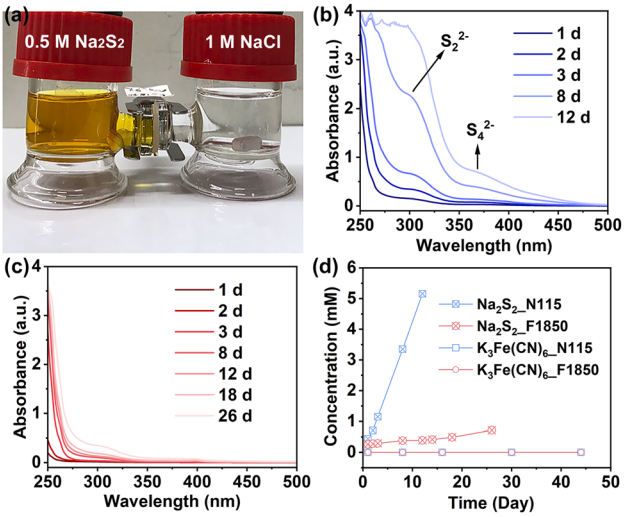

Fig. 1 (a) A digital photo of the permeation cell; (b) UV-vis spectra of permeated Na_2S_2 through N115 as a function of time in days; (c) UV-vis spectra of permeated Na_2S_2 through F1850; (d) the obtained Na_2S_2 and $K_3Fe(CN)_6$ crossover concentrations as a function of test time.

As plotted in Fig. 1d, the F1850 membrane demonstrated a significantly improved polysulfide blocking ability compared to N115. The permeability of S_2^{2-} through F1850 was determined to be 3.15×10^{-6} cm^2 per day (according to Fig. S2c and d†), which is a nearly 100-fold reduction compared to that through N115 (2.12×10^{-4} cm^2 per day). These values are comparable to, or even better than, those of the newly developed CRIS and semi-fluorinated polymer membranes.[19,38] In addition, both membranes showed near-zero crossover for the $Fe(CN)_6^{3-}$ catholyte anion (Fig. S1c†), presumably because of its bulky size and high charge density creating a strong Donnan exclusion effect with the membranes. Therefore, the polysulfide permeation will be the dictating factor that controls the stability of S/Fe flow cells and enhanced cycling performance is expected for F1850.

3.2 Membrane characterization

According to the microheterogeneous model of CEMs,[39] a major composition of the hydrated internal microstructure is interstitial void phases that are filled with an electroneutral electrolyte solution containing cations and a smaller amount of anions (polysulfides in our case). Ion conduction is realized by cation diffusion through the void phases, while anion leakage or crossover is caused by the diffusion of polysulfides across the membrane. The size and spacing of hydrophilic domains (or water clusters) determine the conductivity and permselectivity of a membrane. To account for the enhanced polysulfide blocking ability, the hydrophilic domains in F1850 are expected

Table 1 The relevant parameters of N115 and F1850 membranes

	Thickness (μm)	IEC[a] (meq g^{-1})	EW[a] (g mol^{-1})	WU (%)	SR (%)	Resistivity (Ω cm^2)	Conductivity (mS cm^{-1})
N115	127	0.91	1100	39	10.6	4.83	2.63
F1850	50	0.56	1800	3.9	4.1	21.58	0.23

[a] Obtained from the vendors' product specs.[41]

to have a smaller size and larger spacing than those in N115. To test this argument, we carried out a series of analytical characterizations of these two membranes to understand the intrinsic microstructural origins.

The amount of water adsorbed by the membrane and the extent of dimensional swelling upon hydration reflect the size of water clusters. As shown in Table 1, the K^+-form F1850 exhibits a water uptake (WU) of 3.9% and a swelling ratio (SR) of 4.1%, both of which are substantially lower than those of N115, indicating a lower volumetric presence of hydrophilic domains. As a result, cation transport through F1850 encounters a higher areal resistivity (Fig. S3†) and so does the polysulfide crossover (Fig. 1). Fig. 2a indicates the measured contact angles of 90° and 54° for K^+-form F1850 and N115, respectively. Thus, F1850 exhibits an inferior surface wettability by water due to the higher hydrophobicity, which helps maintain low dimensional expansion upon hydration. FE-SEM images of dry membranes shown in Fig. 2b and c exhibit substantially different morphologies. N115 has a uniform, smooth surface, while F1850 exhibits a rough texture with randomly distributed circular bumps of *ca.* 2–10 microns. However, the formation mechanism for these bumps remains unclear but is speculated to be associated with the phase separation behaviors in F1850's microstructure. Due to the large scan areas, FE-SEM is unable to image nm-sized ion clusters even with an expanded view (Fig. 2c inset). Taking advantage of the good spatial resolution, AFM topography was used to analyze the membrane surface morphologies over smaller scan areas (Fig. 2d and e). A direct observation is that F1850 still has a higher surface roughness than N115 within the much smaller areal dimensions, which agrees with the FE-SEM analysis. The dark and bright colors are considered to represent the hydrophilic and hydrophobic domains, respectively.[40] In N117, the hydrophilic regions are well interconnected aggregating into continuous ion channels of relatively large sizes. In contrast, in F1850, the hydrophilic domains are more substantially separated from each other, resulting in reduced interconnections and smaller dark regions. The surface microphase characteristics can explain the pronounced differences in ionic conductivity and polysulfide permeation between these two membranes.

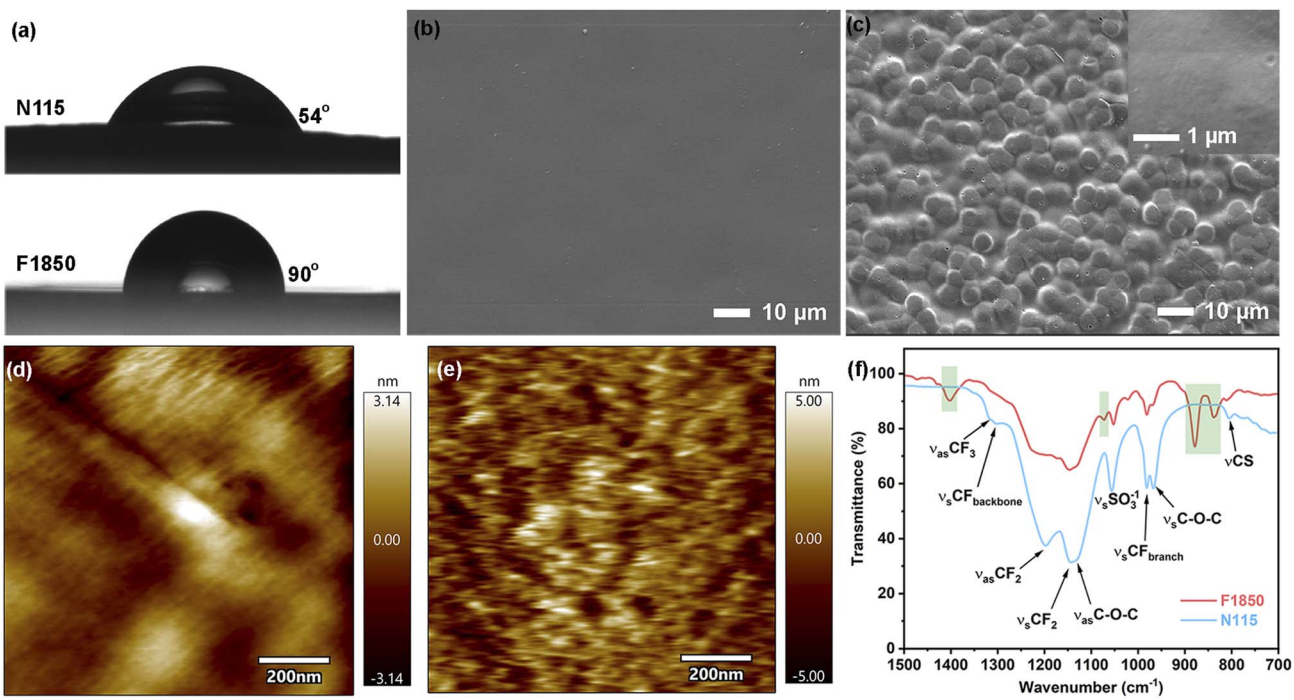

Fig. 2 Membrane characterizations: (a) contact angle; (b) FE-SEM image of N115; (c) FE-SEM image of F1850; (d) tapping-mode AFM image of N115; (e) tapping-mode AFM image of F1850; (f) ATR-FTIR spectra of N115 and F1850.

To obtain fundamental insights into the superior polysulfide retention of F1850, solid-state MAS-NMR was used to characterize the microstructure of this membrane. Fig. 3 shows the ^{19}F NMR spectra as well as the computed deconvolutions with chemical shift assignments to the various C–F groups in polymer structure (inset; see also Tables S1 and S2†). The nature and number of the peaks, including the linewidths, for N115 are broadly consistent with past, detailed NMR studies of Nafion polymer structure,[26,28] with primary resonances for the $\{CF_2\}_n$ peaks (overlapped with the S–CF_2–C signal), the O–CF_2–C signal (overlapped with the pendant –CF_3 signal), and resonances for the –CF– signals at comparatively more negative ppm values (separate signals occur for the backbone and sidechain cases). Conversely, the F1850 structure exhibits a far greater variety of signals, particularly for the shift region associated with the signals from the pendant ionomer sidechains (which are deshielded relative to the backbone signals owing to the proximity to the ether linkages and the terminal sulfonyl groups). Peak assignments are made by a combination of contrasting with prior literature on Nafion's ^{19}F MAS-NMR, comparing across MAS rates to identify spinning sidebands (Fig. S4†), and comparison of linewidths, which derive from a combination of conformational disorder and local dynamical mobility (*i.e.* ^{19}F peaks of –CF_3 rotors are narrow; ^{19}F peaks near the bulky sulfonyl groups are comparatively broader). A similar proliferation of the observed signals for F1850 relative to N115 also occurs from the ^{19}F–^{13}C cross-polarization (CP) spectra (Fig. S5†).

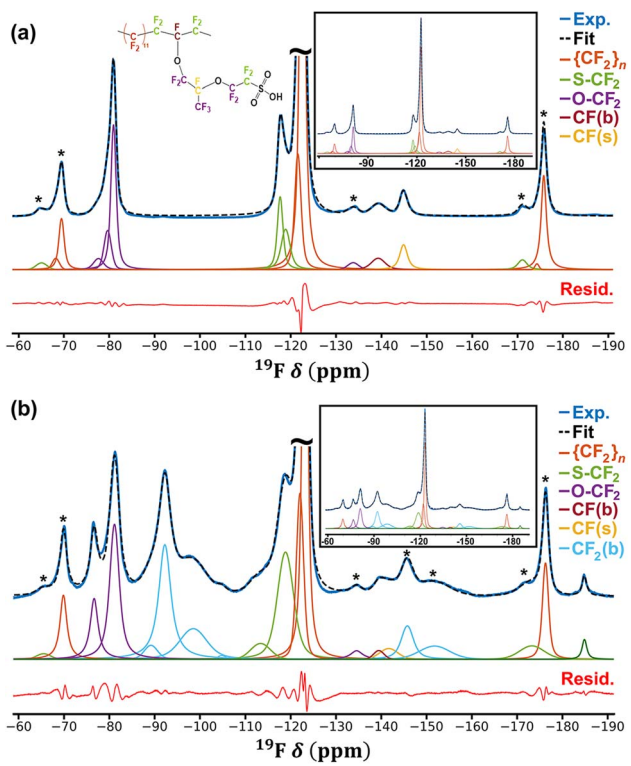

Fig. 3 ^{19}F MAS-NMR: (a) N115 and (b) F1850. Insets give the structural assignment of N115 following ref. 28 and the spectra at full zoom without truncation of the $\{CF_2\}_n$ peaks. Deconvolution components are color-coded to the assignments, as given in the legends. Note for F1850 the appearance of additional signals in the sidechain –CF_2– region (cyan), with broader linewidths consistent with the identified sidechain –CF_2– resonances for N115.

When contrasting the backbone and sidechain signals for N115, the signals attributed to the former yield a total fraction of 0.75 of the total ^{19}F signal, including sidebands ($S_{backbone} = S_{-123} + (4/6)S_{-118} + S_{-139}$), *versus* 0.25 for the sidechains ($S_{sidechain} = S_{-81} + (2/6)S_{-118} + S_{-145}$). In contrast, applying the same calculation for assignable signals in F1850 yields $S_{backbone} = 0.51$ and $S_{sidechain} = 0.21$, leaving a considerable unassigned fraction, which is also difficult to directly link to the putative sidechain structure of F1850, whether a high degree of crosslinking[42] is assumed or otherwise. The ^{19}F–^{13}C CP also indicates, based on the chemical shift range and in comparison with N115, that much of these extra signals are associated with the sidechains, and may involve some degree of branching. A detailed mapping of this unassigned fraction by spectroscopic methods would require extensive use of correlation and recoupling NMR experiments,[28] and is beyond the scope of this study. If, instead, all of the signals are grouped by narrow *versus* broad linewidths, noting that for N115 the linewidths readily partition into a group with <1500 Hz and >1500 Hz (see Table S1†), N115 has a proportion of 0.85 : 0.15, narrow-to-broad, whereas F1850 yields 0.57 : 0.43 for the same. The linewidth can therefore be employed as a measure of relative configurational disorder (*i.e.* an approximate metric for the density/tortuosity of the corresponding membrane), furnishing a means of linking the microstructural characteristics of the membrane to its ability to ensnare large, solvated species and thereby mitigate crossover. By this lens, F1850 intrinsically differs from N115, particularly with regard to its sidechain moieties (based on the typical chemical shift range of the unassigned signals for both ^{19}F and ^{13}C). This added sidechain disorder and potential branching/pseudo-crosslinking may restrict the freedom of microphase separation, congest the ion channels, and limit their permeability to polysulfide species. Correspondingly, this will also limit the volumetric extent of the hydrophilic domains in the membrane *via* the additional complexity of the sidechain interactions/tangling, which will reduce the mean free path of diffusing polysulfide species and attenuate their traversal of the full breadth of the membrane.

ATR-FTIR analysis was then carried out to identify the different structural features in F1850. The ATR-FTIR spectra and the assignment of major peaks of F1850 and N115 membranes are displayed in Fig. 2f. Nafion membranes have been extensively characterized by this technique and our result agrees well with the previously obtained examples,[43–45] which assisted with the peak assignments. First, the major peaks of N115 also occur in F1850 with similar patterns, including $\nu_{as}CF_3$ at 1319 cm^{-1}, $\nu_sCF_{backbone}$ at 1304 cm^{-1}, $\nu_{as}CF_2$ at 1197 cm^{-1}, ν_sCF_2 at 1143 cm^{-1}, ν_{as}C–O–C at 1134 cm^{-1}, $\nu_sSO_3^-$ at 1056 cm^{-1}, ν_sCF_{branch} at 982 cm^{-1}, and ν_sC–O–C at 967 cm^{-1}. Second, a few new peaks are observed in F1850, such as those highlighted by green boxes at 1403, 1073, 878, and 837 cm^{-1}. These new features point to the major structural differences between F1850 and N115, which may be associated with the

more disordered sidechain of F1850. However, it remains a challenge to precisely identify these functionalities in the polymer.

3.3 Electrochemical test

To verify the electrochemical activities, cyclic voltammetry (CV) curves of both $K_3Fe(CN)_6$ and Na_2S_2 were collected using respectively relevant working electrodes. A glassy carbon electrode was used for $K_3Fe(CN)_6$ to measure a redox potential of 0.26 V *vs.* Ag/AgCl (Fig. 4). With combined Randles–Sevcik and Nicholson analyses of CV scans of 50 mM $K_3Fe(CN)_6$ (Fig. S6†), $K_3Fe(CN)_6$ exhibited a diffusion coefficient (D) of 2.89×10^{-6} $cm^2\ s^{-1}$ and an electrochemical rate constant (k_0) of 2.86×10^{-3} cm s^{-1}, which agree well with prior studies.[24] Co-electrodeposited glassy carbon was used for Na_2S_2, as Co metal has been established as an effective electrocatalyst for polysulfide redox.[14,30,31] Electrodeposition of the Co coating on the glassy carbon surface was performed through holding a constant potential at approximately −0.5 V lower than the Co deposition potential for 20 seconds (Fig. S7†). The electrochemistry of the polysulfide is more complex due to the possibility of concurrent conversion to polysulfide ions of various lengths. Multiple redox peaks have been commonly observed in carbon working electrode-based CV studies,[14,18,46–48] which makes the peak assignments uncertain. As shown in Fig. 4, Na_2S_2 showed the major oxidation and reduction peaks at −0.16 V and −0.95 V *vs.* Ag/AgCl, respectively. Even with the Co catalyst, the wide peak separation reflects the slow redox kinetics of polysulfide conversion, which is another critical challenge for polysulfide-based RFBs. A few minor peaks were detected at −0.58, −0.63, and −0.82 V *vs.* Ag/AgCl but it is difficult to assign their identities accurately. This voltametric complication reflects the likely involvement of more polysulfide species and chemical reactions during the electrochemical conversion process. The substantially higher current of Na_2S_2 than that of $K_3Fe(CN)_6$ measured at the same concentration is presumably ascribed to the higher number of transferred electrons during their redox reactions.

The permeation tests have offered a preliminary indication of the membranes' polysulfide retention abilities under simplified conditions where the concentration gradient across the membrane is the major driving force for crossover. Flow cell cycling involves additional operation factors that may exaggerate polysulfide crossover, such as the presence of an electric field, active Na^+/K^+ transport, electrolyte circulation, different counter-electrolyte settings, *etc.* To demonstrate the practical feasibility of F1850, the S/Fe flow cells assembled with this membrane were evaluated under RFB-relevant conditions. Again, N115 was tested as the baseline.

The sluggish redox kinetics of polysulfide conversion requires the use of an electrocatalyst-decorated porous electrode in flow cells. The cobalt-decorated SIGRACELL® graphite felt electrodes (Co/GFD2.5) were prepared by thermally reducing the $Co(NO_3)_2$-impregnated GFD2.5 in a 4% H_2/argon atmosphere. A Co loading of 11.6 mg cm^{-2} was obtained. The morphology of the Co coating is revealed with FE-SEM and is shown in Fig. S8.† Irregularly shaped Co clusters sized at several tens of microns are randomly distributed on carbon fibers. Micron-scale etches on the fiber surface are also observed in the FE-SEM image. These functional modifications boost the surface area of the electrode structure and increase the active sites for electrocatalysis.

The S/Fe flow cells with F1850 and N115, respectively, were assembled in the fully charged state with 1 M Na_2S_2 anolyte and 1 M $K_3Fe(CN)_6$ catholyte (Fig. 5a). The use of mixed Na^+ and K^+ cations has been reported capable of boosting the solubility of $K_4Fe(CN)_6$ from ~0.7 M up to ~1.5 M.[49,50] In the flow cell, the through-membrane transport of Na^+ and K^+ ions will result in mixed cations. Therefore, cycling with 1 M catholyte will not cause precipitation of $K_4Fe(CN)_6$, which was demonstrated in

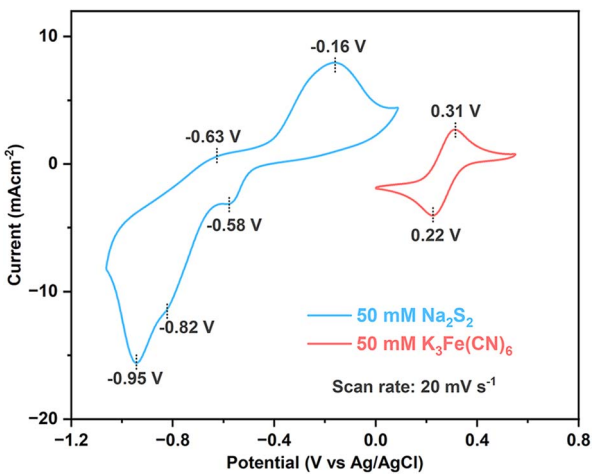

Fig. 4 CV curves of 50 mM $K_3Fe(CN)_6$ and 50 mM Na_2S_2, respectively, in 1 M supporting salts at 20 mV s^{-1}.

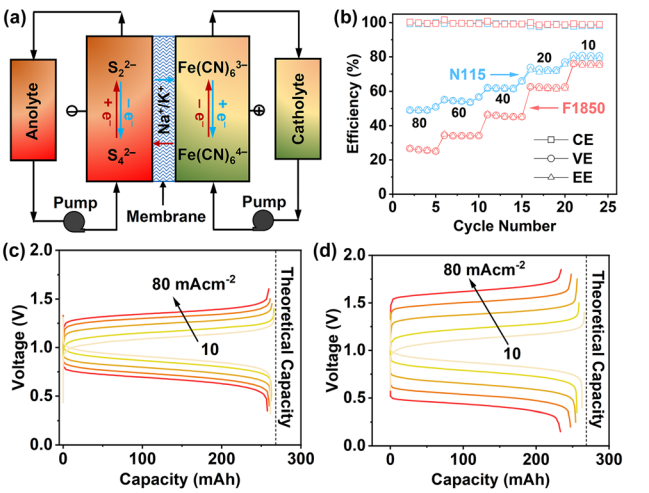

Fig. 5 (a) An illustration of the S/Fe flow cell; (b) rate capability of S/Fe flow cells using F1850 and N115 membranes. Voltage curves at different current densities of S/Fe flow cells using (c) N115 and (d) F1850. The anolyte was 1 M Na_2S_2 and the catholyte was 1 M $K_3Fe(CN)_6$.

a previous report under similar conditions.[14] Fig. S9† shows the Nyquist plots and the fitting with the classical Thevenin equivalent circuit model. F1850 yielded a higher ohmic ASR (R_Ω, 6.34 Ω cm^2) than N115 (2.77 Ω cm^2) to the S/Fe flow cell, and the charge transfer resistivities (R_{CT}) were similar (~0.4 Ω cm^2) for these two membranes. Thus, the R_Ω appeared to dictate the flow cell efficiency. As shown in Fig. 5b, F1850 exhibited an inferior rate capability compared to N115 under the same test conditions. For the F1850-based flow cell, as the current density increased from 10 to 80 mA cm^{-2}, the voltage efficiency (VE) was decreased from 75.9% to 25.6% and the energy efficiency (EE) from 75.0% to 25.5%. The catholyte material utilization, based on the discharge capacity, was generally high and slightly dropped from 98.0% to 85.3% with the current density. In contrast, the N115-based flow cell showed decreases in VE from 80.6% to 49.1%, in EE from 79.1% to 48.8%, and in catholyte utilization from 96.1% to 89.7%. In addition, F1850 generally afforded higher coulombic efficiencies (CEs) than N115 at these current densities, which agrees well with the better polysulfide blocking ability of the former membrane. Well-defined single plateaus were observed in the voltage curves of both flow cells at these tested current densities (Fig. 5c and d), although multiple redox peaks were seen in the CV curve of polysulfides (Fig. 4). This is because stoichiometrically excessive polysulfide was used to compensate for its probable crossover loss during cycling. Such electrolyte settings have been commonly used for the testing of polysulfide RFBs in most of the reported studies.

Long-term cyclability is particularly important for bestowing polysulfide RFBs with commercialization relevance. The better polysulfide blocking ability of the F1850 membrane is expected to lead to more stable cycling. To test this hypothesis, continuous galvanostatic cycling at a constant current density of 20 mA cm^{-2} was carried out on the S/Fe flow cells. Fig. 6a displays the cycling efficiencies and capacities as functions of cycle number and test time for the F1850-based S/Fe flow cell. With an average CE of 99.2% and EE of 62.5%, the flow cell demonstrated a stable capacity profile for approximately 300 cycles over a test time of 49 days, leading to an average capacity fading rate as low as 0.029% per cycle and 0.176% per day. In contrast, the parallel test with N115 yielded a CE of 98.5% and remained stable for only 120 cycles and 19 days (Fig. 6b). Such an extended time duration with the well-maintained capacity at ~97% SOC reflects the inherent polysulfide retention attribute of F1850. This performance is significantly better than that of most reported polysulfide RFBs and places F1850 as an exceeding candidate for permselective membranes. The cycling results confirm our claim of the favorable properties of F1850 toward advancing polysulfide-based RFBs.

It is noted that the VEs of both flow cells were continuously decreased as the cycling proceeded. From the voltage curves of selected cycles, gradual increases in the cell overpotential were observed over the course of the test (Fig. S10†). The major reason for this phenomenon is polysulfide crossover. The leaked polysulfide reacted with the $K_3Fe(CN)_6$ catholyte forming an insulating elemental sulfur solid on the surfaces of the GFD2.5 electrode and membrane. The sulfur deposition occurred way before the capacity started to fade. According to the FE-SEM images and EDX sulfur mapping shown in Fig. S11,† sparsely distributed sulfur deposits were already non-negligible at the 120th cycle for the F1850-based S/Fe flow cell. The accumulation of sulfur on the electrode surface eventually resulted in fluctuations or fading of the capacity and efficiency. After a 30% loss of the capacity at the 530th cycle (*i.e.*, the ~80th day), sulfur particles were detected at the catholyte side – on the membrane and inside the electrode (Fig. S12†). For the N115-based flow cell, sulfur deposition was even more serious. Thick layers of sulfur were visually observed at the catholyte side after only 39 days of cycling when the capacity faded to ~30% of the initial value (Fig. S13†). Clogging of the flow path can be easily envisaged.

An additional note is that the cycling stability is moderately affected by the polysulfide ion size, which was demonstrated in N115-based S/Fe flow cells. When polysulfides of different chain lengths were used (in large excess) under otherwise identical conditions, different cycling results were obtained. As shown in Fig. S14,† the S_4^{2-}/$Fe(CN)_6^{4-}$ flow cell maintained stable capacity for a moderately longer duration of 24 days (*i.e.*, 125 cycles). In stark contrast, rapid capacity degradation was identified for the S^{2-}/$Fe(CN)_6^{3-}$ flow cell. Intuitively, this result is primarily because the smaller polysulfide size allows easier access into the transport channels in the membrane. Yet, other factors may simultaneously play a role in causing the unstable

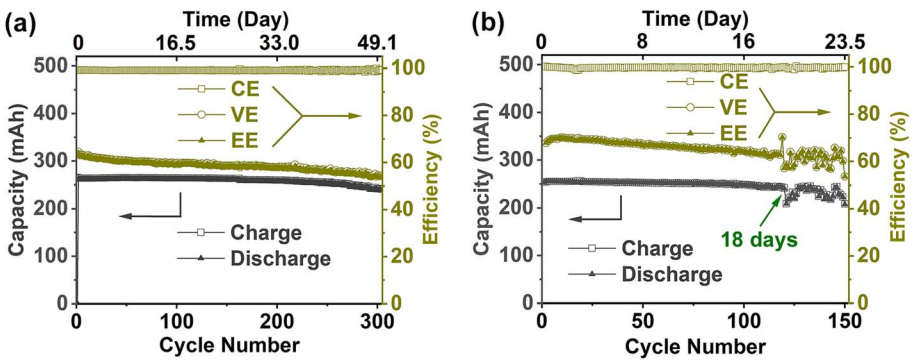

Fig. 6 Long cycling of S/Fe flow cells using (a) F1850 and (b) N115 at 20 mA cm^{-2}. The anolyte was 1 M Na_2S_2 (15 mL) and the catholyte was 1 M $K_3Fe(CN)_6$ (10 mL).

capacity. It's been reported that S^{2-} is more vulnerable than longer polysulfides to hydrolysis forming HS^- or even gaseous H_2S, which is a known origin of the chemical instability of monosulfides in near-pH-neutral solutions.[51–53] This adverse effect may explain the drastically different capacity behavior of the $S^{2-}/Fe(CN)_6^{3-}$ flow cell, *i.e.*, the continuous capacity fading even from the first cycle. This possibility also highlights the necessary electrolyte control to maintain the chemical stability of polysulfides.[12] Nevertheless, a potential implication from the only mild improvement in cyclability is that electrolyte engineering aimed at enhancing polysulfide retention should rely more on other electrolyte factors than on polysulfides themselves.

4. Conclusions

In conclusion, we have demonstrated the positive effects of the improved membrane permselectivity on mitigation of polysulfide leakage in aqueous RFBs. The smaller ion channel size in the F1850 membrane compared to Nafion is demonstrated by correlated water adsorption, dimensional swelling, ionic conductivity, contact angle, FE-SEM, AFM, ATR-FTIR, and MAS-NMR characterizations. The enhanced polysulfide retention ability of F1850 has been evinced in both permeation cells and S/Fe flow cells. The crossover flux of polysulfides was reduced by nearly two orders of magnitude compared to that of the widely used Nafion membrane under non-flow conditions. Despite the price of compromised efficiencies, the cycling stability of S/Fe flow cells was boosted over an extended time duration of 49 days. This finding indicates a potential membrane strategy to foster the observed selective ion transport and address the long-standing irreversible polysulfide crossover challenge.

We should point out that this F1850 membrane is limited by the well-known conductivity–selectivity trade-off in ion exchange membranes. Because slow kinetics is also a critical challenge for polysulfide redox, the reduced membrane conductivity aggravates the low efficiency issue of polysulfide RFBs. Therefore, advanced membrane approaches need to be developed to achieve both selectivity and conductivity simultaneously.

Data availability

The data presented in this article are in the format of figures. The data supporting this article have been included as part of the ESI.†

Author contributions

Conceptualization, X. W.; investigation, M. S. K., A. T., D. M., S. B., B. M., J. P. M., G. P., H. Z., X. Z., J. D. B.; resources, A. T., M. A., H. Z., X. Z., J. D. B., X. W.; data curation, X. Z., J. D. B., X. W.; writing—original draft preparation, M. S. K., X. W.; writing—review and editing, M. S. K., A. T., D. M., S. B., X. Z., J. D. B., X. W.; visualization, M. S. K., X. W.; supervision, X. W.; project administration, X. W.; funding acquisition, X. W. All authors have read and agreed to the published version of the manuscript.

Conflicts of interest

There are no conflicts to declare.

Acknowledgements

This work was supported by the U.S. National Science Foundation (Award No. CHE-2055222). The solid-state NMR measurements were performed with a capacity time award (DOI: https://doi.org/10.46936/cpcy.proj.2022.60601/60008671) from the Environmental and Molecular Sciences Laboratory, a DOE User Facility based at Pacific Northwest National Laboratory. X. Z. also acknowledges support from the U.S. Department of Energy (DOE), Office of Science, Basic Energy Sciences (BES), Chemical Sciences, Geosciences, and Biosciences Division through its Geosciences Program at Pacific Northwest National Laboratory (FWP 56674).

Notes and references

1 M. I. Fernandez, Y. I. Go, D. M. L. Wong and W.-G. Früh, Review of challenges and key enablers in energy systems towards net zero target: Renewables, storage, buildings, & grid technologies, *Heliyon*, 2024, **10**(23), e40691, DOI: 10.1016/j.heliyon.2024.e40691.

2 S. J. Russell and P. Norvig, *Artificial Intelligence: a Modern Approach*, Pearson, 2016.

3 R. Shan, J. Reagan, S. Castellanos, S. Kurtz and N. Kittner, Evaluating emerging long-duration energy storage technologies, *Renewable Sustainable Energy Rev.*, 2022, **159**, ARTN112240, DOI: 10.1016/j.rser.2022.112240.

4 G. L. Soloveichik, Flow Batteries: Current Status and Trends, *Chem. Rev.*, 2015, **115**(20), 11533–11558, DOI: 10.1021/cr500720t.

5 R. M. Darling, K. G. Gallagher, J. A. Kowalski, S. Ha and F. R. Brushett, Pathways to low-cost electrochemical energy storage: a comparison of aqueous and nonaqueous flow batteries, *Energy Environ. Sci.*, 2014, **7**(11), 3459–3477, DOI: 10.1039/c4ee02158d.

6 K. Lourenssen, J. Williams, F. Ahmadpour, R. Clemmer and S. Tasnim, Vanadium redox flow batteries: A comprehensive review, *J. Energy Storage*, 2019, **25**, 100844.

7 J. Winsberg, T. Hagemann, T. Janoschka, M. D. Hager and U. S. Schubert, Redox-Flow Batteries: From Metals to Organic Redox-Active Materials, *Angew. Chem., Int. Ed.*, 2017, **56**, 686–711, DOI: 10.1002/anie.201604925.

8 J. A. Luo, B. Hu, M. W. Hu, Y. Zhao and T. L. Liu, Status and Prospects of Organic Redox Flow Batteries toward Sustainable Energy Storage, *ACS Energy Lett.*, 2019, **4**(9), 2220–2240, DOI: 10.1021/acsenergylett.9b01332.

9 J. Y. Cao, J. Y. Tian, J. Xu and Y. G. Wang, Organic Flow Batteries: Recent Progress and Perspectives, *Energy Fuels*, 2020, **34**(11), 13384–13411, DOI: 10.1021/acs.energyfuels.0c02855.

10 S. P. Zhang, W. J. Guo, F. C. Yang, P. N. Zheng, R. Qiao and Z. Li, Recent Progress in Polysulfide Redox-Flow Batteries, *Batteries Supercaps*, 2019, **2**(7), 627–637, DOI: 10.1002/batt.201900056.

11 B. Li and J. Liu, Progress and directions in low-cost redox-flow batteries for large-scale energy storage, *Natl. Sci. Rev.*, 2017, **4**(1), 91–105, DOI: 10.1093/nsr/nww098.

12 M. Sarfaraz Khabbaz, S. Biabanialitappeh and X. Wei, Electrocatalysts and Membranes for Aqueous Polysulfide Redox Flow Batteries, *ACS Nano*, 2025, **19**(22), 20321–20356, DOI: 10.1021/acsnano.5c00872.

13 P. Morrissey, An Overview of the Polysulfide/Bromine Flow Battery, in *Flow Batteries: from Fundamentals to Applications*, ed. Roth C., Noack J. and Skyllas-Kazacos M., WILEY-VCH GmbH, 1st edn, 2023, pp. 765–790.

14 X. L. Wei, G. G. Xia, B. Kirby, E. Thomsen, B. Li, Z. M. Nie, G. G. Graff, J. Liu, V. Sprenkle and W. Wang, An Aqueous Redox Flow Battery Based on Neutral Alkali Metal Ferri/ferrocyanide and Polysulfide Electrolytes, *J. Electrochem. Soc.*, 2016, **163**(1), A5150–A5153, DOI: 10.1149/2.0221601jes.

15 L. Su, A. F. Badel, C. Cao, J. J. Hinricher and F. R. Brushett, Toward an inexpensive aqueous polysulfide–polyiodide redox flow battery, *Ind. Eng. Chem. Res.*, 2017, **56**(35), 9783–9792.

16 M. Ding, H. Fu, X. Lou, M. He, B. Chen, Z. Han, S. Chu, B. Lu, G. Zhou and C. Jia, A Stable and Energy-Dense Polysulfide/Permanganate Flow Battery, *ACS Nano*, 2023, **17**(16), 16252–16263, DOI: 10.1021/acsnano.3c06273.

17 Z. Li, G. Weng, Q. Zou, G. Cong and Y.-C. Lu, A high-energy and low-cost polysulfide/iodide redox flow battery, *Nano Energy*, 2016, **30**, 283–292.

18 D. Ma, B. Hu, W. Wu, X. Liu, J. Zai, C. Shu, T. Tadesse Tsega, L. Chen, X. Qian and T. L. Liu, Highly active nanostructured CoS2/CoS heterojunction electrocatalysts for aqueous polysulfide/iodide redox flow batteries, *Nat. Commun.*, 2019, **10**(1), 3367.

19 Z. J. Li and Y. C. Lu, Polysulfide-based redox flow batteries with long life and low levelized cost enabled by charge-reinforced ion-selective membranes, *Nat. Energy*, 2021, **6**(5), 517–528, DOI: 10.1038/s41560-021-00804-x.

20 B. X. Chen, H. Huang, J. D. Lin, K. L. Zhu, L. Yang, X. Wang and J. J. Chen, Doping Engineering of M-N-C Electrocatalyst Based Membrane-Electrode Assembly for High-Performance Aqueous Polysulfides Redox Flow Batteries, *Adv. Sci.*, 2023, **10**(16), ARTN2206949, DOI: 10.1002/advs.202206949.

21 J. Lan, K. Li, L. Yang, Q. Lin, J. Duan, S. Zhang, X. Wang and J. Chen, Hierarchical nano-electrocatalytic reactor for high performance polysulfides redox flow batteries, *ACS Nano*, 2023, **17**(20), 20492–20501, DOI: 10.1021/acsnano.3c07085.

22 Y. H. Xia, M. Z. Ouyang, V. Yufit, R. Tan, A. Regoutz, A. Q. Wang, W. J. Mao, B. Chakrabarti, A. Kavei, Q. L. Song, *et al.*, A cost-effective alkaline polysulfide-air redox flow battery enabled by a dual-membrane cell architecture, *Nat. Commun.*, 2022, **13**(1), ARTN2388, DOI: 10.1038/s41467-022-30044-w.

23 Z. Li, M. S. Pan, L. Su, P.-C. Tsai, A. F. Badel, J. M. Valle, S. L. Eiler, K. Xiang, F. R. Brushett and Y.-M. Chiang, Air-breathing aqueous sulfur flow battery for ultralow-cost long-duration electrical storage, *Joule*, 2017, **1**(2), 306–327.

24 J. Luo, A. Sam, B. Hu, C. DeBruler, X. L. Wei, W. Wang and T. L. Liu, Unraveling pH dependent cycling stability of ferricyanide/ferrocyanide in redox flow batteries, *Nano Energy*, 2017, **42**, 215–221, DOI: 10.1016/j.nanoen.2017.10.057.

25 E. M. Fell, D. De Porcellinis, Y. Jing, V. Gutierrez-Venegas, T. Y. George, R. G. Gordon, S. Granados-Focil and M. J. Aziz, Long-Term Stability of Ferri-/Ferrocyanide as an Electroactive Component for Redox Flow Battery Applications: On the Origin of Apparent Capacity Fade, *J. Electrochem. Soc.*, 2023, **170**(7), 070525, DOI: 10.1149/1945-7111/ace936.

26 M. Vijayakumar, Q. T. Luo, R. Lloyd, Z. M. Nie, X. L. Wei, B. Li, V. Sprenkle, J. D. Londono, M. Unlu and W. Wang, Tuning the Perfluorosulfonic Acid Membrane Morphology for Vanadium Redox-Flow Batteries, *ACS Appl. Mater. Interfaces*, 2016, **8**(50), 34327–34334, DOI: 10.1021/acsami.6b10744.

27 S. G. J. van Meerten, W. M. J. Franssen and A. P. M. Kentgens, ssNake: A cross-platform open-source NMR data processing and fitting application, *J. Magn. Reson.*, 2019, **301**, 56–66, DOI: 10.1016/j.jmr.2019.02.006.

28 Q. Chen and K. Schmidt-Rohr, 19F and 13C NMR signal assignment and analysis in a perfluorinated ionomer (Nafion) by two-dimensional solid-state NMR, *Macromolecules*, 2004, **37**(16), 5995–6003.

29 R. G. Compton and C. E. Banks, *Understanding Voltammetry*, World Scientific, 2018.

30 H. T. Zhou, H. M. Zhang, P. Zhao and B. L. Yi, Novel cobalt coated carbon felt as high performance negative electrode in sodium polysulfide/bromine redox flow battery, *Electrochemistry*, 2006, **74**(4), 296–298.

31 Z. Yang, M. R. Gerhardt, M. Fortin, C. Shovlin, A. Z. Weber, M. L. Perry, R. M. Darling and J. D. Saraidaridis, Polysulfide-permanganate flow battery using abundant active materials, *J. Electrochem. Soc.*, 2021, **168**(7), 070516.

32 J. Vrána, J. Charvát, P. Mazúr, P. Bělský, J. Dundálek, J. Pocedič and J. Kosek, Commercial perfluorosulfonic acid membranes for vanadium redox flow battery: Effect of ion-exchange capacity and membrane internal structure, *J. Membr. Sci.*, 2018, **552**, 202–212, DOI: 10.1016/j.memsci.2018.02.011.

33 V. Baglio, A. Stassi, O. Barbera, G. Giacoppo, D. Sebastian, C. D'Urso, M. Schuster, B. Bauer, J. L. Bonde and A. S. Aricò, Direct methanol fuel cell stack for auxiliary power units applications based on fumapem® F-1850 membrane, *Int. J. Hydrogen Energy*, 2017, **42**(43), 26889–26896, DOI: 10.1016/j.ijhydene.2017.08.109.

34 A. S. Aricò, D. Sebastian, M. Schuster, B. Bauer, C. Urso, F. Lufrano and V. Baglio, Selectivity of Direct Methanol Fuel Cell Membranes, *Membranes*, 2015, **5**(4), 793–809, DOI: 10.3390/membranes5040793.

35 V. Viswanathan, A. Crawford, D. Stephenson, S. Kim, W. Wang, B. Li, G. Coffey, E. Thomsen, G. Graff, P. Balducci, *et al.*, Cost and performance model for redox

flow batteries, *J. Power Sources*, 2014, **247**, 1040–1051, DOI: 10.1016/j.jpowsour.2012.12.023.

36 R. Steudel, Inorganic polysulfides S_n^{2-} and radical anions $Sn^{\cdot-}$, *Elemental Sulfur und Sulfur-Rich Compounds II*, 2003, pp. 127–152.

37 A. Kamyshny, A. Goifman, J. Gun, D. Rizkov and O. Lev, Equilibrium distribution of polysulfide ions in aqueous solutions at 25 C: a new approach for the study of polysulfides' equilibria, *Environ. Sci. Technol.*, 2004, **38**(24), 6633–6644.

38 S. Sreenath, P. S. Nayanthara, C. M. Pawar, A. Ash, B. Bhatt, V. Verma and R. K. Nagarale, An aqueous polysulfide redox flow battery with a semi-fluorinated cation exchange membrane, *Energy Adv.*, 2024, **3**(1), 203–214.

39 V. I. Zabolotsky and V. V. Nikonenko, Effect of structural membrane inhomogeneity on transport properties, *J. Membr. Sci.*, 1993, **79**(2–3), 181–198.

40 Y. Zhu, L. Ding, X. Liang, M. A. Shehzad, L. Wang, X. Ge, Y. He, L. Wu, J. R. Varcoe and T. Xu, Beneficial use of rotatable-spacer side-chains in alkaline anion exchange membranes for fuel cells, *Energy Environ. Sci.*, 2018, **11**(12), 3472–3479, DOI: 10.1039/C8EE02071J.

41 N115, https://ion-power.com/membranes/, accessed on 04/24/2025, F1850: https://www.fuelcellstore.com/spec-sheets/fumasep-f-1850-technical-specifications.pdf, accessed on 04/24/2025.

42 Y. M. Zhang, L. Li, J. Tang, B. Bauer, W. Zhang, H. R. Gao, M. Taillades-Jacquin, D. J. Jones, J. Rozière and N. Lebedeva, Development of covalently cross-linked and composite perfluorosulfonic acid membranes, *ECS Trans.*, 2009, **25**(1), 1469.

43 Z. Liang, W. Chen, J. Liu, S. Wang, Z. Zhou, W. Li, G. Sun and Q. Xin, FT-IR study of the microstructure of Nafion® membrane, *J. Membr. Sci.*, 2004, **233**(1), 39–44, DOI: 10.1016/j.memsci.2003.12.008.

44 M. Danilczuk, L. Lin, S. Schlick, S. J. Hamrock and M. S. Schaberg, Understanding the fingerprint region in the infra-red spectra of perfluorinated ionomer membranes and corresponding model compounds: Experiments and theoretical calculations, *J. Power Sources*, 2011, **196**(20), 8216–8224, DOI: 10.1016/j.jpowsour.2011.05.067.

45 A. Gruger, A. Régis, T. Schmatko and P. Colomban, Nanostructure of Nafion® membranes at different states of hydration: An IR and Raman study, *Vib. Spectrosc.*, 2001, **26**(2), 215–225, DOI: 10.1016/S0924-2031(01)00116-3.

46 Y. Qin, X. Li, W. Liu and X. Lei, High-performance aqueous polysulfide-iodide flow battery realized by an efficient bifunctional catalyst based on copper sulfide, *Mater. Today Energy*, 2021, **21**, 100746.

47 X. Lou, H. Fu, J. Xu, Y. Long, S. Yan, H. Zou, B. Lu, M. He, M. Ding and X. Zhu, Cost-effective membrane and advanced electrode for stable polysulfide-ferricyanide flow battery, *Energy Mater. Adv.*, 2022, **2022**, 9865618, DOI: 10.34133/2022/98656.

48 J. Liu, L. Ren, Y. Wang, X. Lu, M. Zhou and W. Liu, A highly-stable bifunctional NiCo2S4 nanoarray@ carbon paper electrode for aqueous polysulfide/iodide redox flow battery, *J. Power Sources*, 2023, **561**, 232607.

49 Y. Long, Z. Z. Xu, G. X. Wang, H. Xu, M. H. Yang, M. Ding, D. Yuan, C. A. W. Yan, Q. J. Sun, M. Liu, *et al.*, A neutral polysulfide/ferricyanide redox flow battery, *Iscience*, 2021, **24**(10), ARTN103157, DOI: 10.1016/j.isci.2021.103157.

50 A. J. Esswein, J. Goeltz and D. Amadeo, High Solubility Iron Hexacyanides, US20140051003A1, 2014.

51 B. Meyer, K. Ward, K. Koshlap and L. Peter, Second dissociation constant of hydrogen sulfide, *Inorg. Chem.*, 1983, **22**(16), 2345–2346, DOI: 10.1021/ic00158a027.

52 S. Licht, K. Longo, D. Peramunage and F. Forouzan, Conductometric analysis of the second acid dissociation constant of H2S in highly concentrated aqueous media, *J. Electroanal. Chem. Interfacial Electrochem.*, 1991, **318**(1), 111–129, DOI: 10.1016/0022-0728(91)85298-4.

53 P. M. May, D. Batka, G. Hefter, E. Königsberger and D. Rowland, Goodbye to S2− in aqueous solution, *Chem. Commun.*, 2018, **54**(16), 1980–1983, DOI: 10.1039/C8CC00187A.

